

Effect of Magnetic Fields on Resonant Solar Acoustic Frequencies



TUNEER CHAKRABORTY

Advisor: Prof. Shravan M Hanasoge

Department of Astronomy and Astrophysics
Tata Institute of Fundamental Research

Submitted in partial fulfilment of the requirement for the degree of
Master of Science

Declaration

I hereby declare that except where specific reference is made to the work of others, the contents of this dissertation are original and have not been submitted in whole or in part for consideration for any other degree or qualification in this, or any other university. This dissertation is my own work and contains nothing which is the outcome of work done in collaboration with others, except as specified in the text, References, and Acknowledgements.

TUNEER CHAKRABORTY
AUGUST 2019

Acknowledgements

I'd like to acknowledge the mentorship and guidance provided by Shravan throughout my last two years as well as in this project. If not for him, I perhaps would not have immersed myself in and missed out on this wonderful subject. I also acknowledge the tireless work and unending enthusiasm of my collaborator, Srijan Bharati Das from Princeton to bring this work to fruition. I also acknowledge many a fruitful discussions we've had with Samarth G K and Dr H M Antia, for getting a handle on solar differential rotation. Finally, I want to thank Sunil Jaiswal, Pranav S, and Samarth GK who proofread the manuscript and significantly uplifted its quality through their invaluable suggestions.

Abstract

This work aims at solving the helioseismic forward problem of finding frequency splittings in of degenerate solar p-modes due to steady global magnetic fields. A integral form of frequency splittings in term of Lorentz stress ($\mathbf{B} \mathbf{B}$) and corresponding sensitivity kernels is proposed. Analytic forms of these kernels are evaluated. A synthetic magnetic field is constructed to validate the sensitivity kernels. It is found that a predominantly toroidal magnetic field of peaking ar $10^5 G$ existing at the tachocline and a dipolar magnetic field ranging from tachocline to surface at $10 G$ introduces a mean shift of about $5 nHz$ and an a_2 of about $60 pHz$ int the splitting profile. These changes in the acoustic frequency spectrum are not detectable by current level of observational precision in helioseismic data.

Table of contents

1	Introduction	1
1.1	What is helioseismology?	1
1.2	Overview	1
2	Formalism	3
2.1	Standard Model and Frequency splittings	3
2.1.1	Background equation of motion	3
2.1.2	Form of eigenfunction	4
2.2	Quasi Degenerate Perturbation Theory	5
2.3	Representation of Splitting Data	6
3	The Rotating Sun	8
3.1	Differential Rotation	8
3.2	Detection from frequency spectrum	8
3.2.1	QDPT Analysis	9
3.2.2	Selecion rules in mode coupling	9
4	Internal Magnetic Fields	12
4.1	Solar Magnetic Field	12
4.2	Equation of Motion	12
4.3	Coupling Matrix	13
4.3.1	Lorentz Stress components	13
4.3.2	Sensitivity Kernels	13
4.4	Synthetic Magnetic Field	16
4.4.1	Construction of \mathbf{B}	16
4.4.2	Construction of \mathcal{H}	17
5	Results	19
5.1	Frequency Splittings due to Differential Rotation	19
5.1.1	Splitting with pure rotation	19
5.1.2	Splitting with pure rotation removed	20
5.2	Splittings due to Lorentz Stresses	21
5.2.1	Detectibility	23
5.3	Conclusion	23

Table of contents

References	26
Appendix A Generalised Spherical Harmonics Formalism	28
A.1 Formalism	28
A.2 Conventions	29
A.3 Spherical triple integral	29
A.4 Rotation	29

Chapter 1

Introduction

1.1 What is helioseismology?

Helioseismology is the study of structure and internal dynamics of the sun as a system by analysing its oscillations. It was discovered in 1960 that a time series of solar dopplegram images reveal global oscillations in line of sight velocity with well defined frequencies [1]. Most of observational helioseismic data is that of oscillations of the of solar material manifesting on the surface [2]. A Dopplergram image is an image of sun formed by measuring doppler shift of a predetermined atomic spectral line and assigning a line-of-sight velocity to the corresponding pixel. After arranging all the pixels one obtains a map of the line of sight velocity of the sun in an instant of time like figure (1.1). A number of dopplergram images can be arranged in time order to form a ‘time series’. This time series allows us to process this data to obtain either frequency spectra (for global helioseismology), or time-distance measurements (for local helioseismology).

Global helioseismology attempts to probe the internal structure of the sun by analysing stochastically excited resonant acoustic modes and their corresponding frequencies. While local helioseismology attempts to achieve this goal via analysis of wavefield cross-correlations and travel times on the solar surface [3].

1.2 Overview

In the second chapter, we motivate and develop the prerequisite techniques which are widely used in the rest of the work. We describe the standard model of the sun that we consider as a background model in this work. Next we describe briefly the method of quasi-degenerate perturbation theory that we use repeatedly to find frequency corrections of closely placed modes as a result of mode-coupling. We also discuss the standard way of representing splitting data in helioseismology.

In the third and fourth chapters, we discuss coupling of modes due to differential rotation and magnetic fields respectively. The last chapter is devoted to quoting and discussing the results of our analysis.

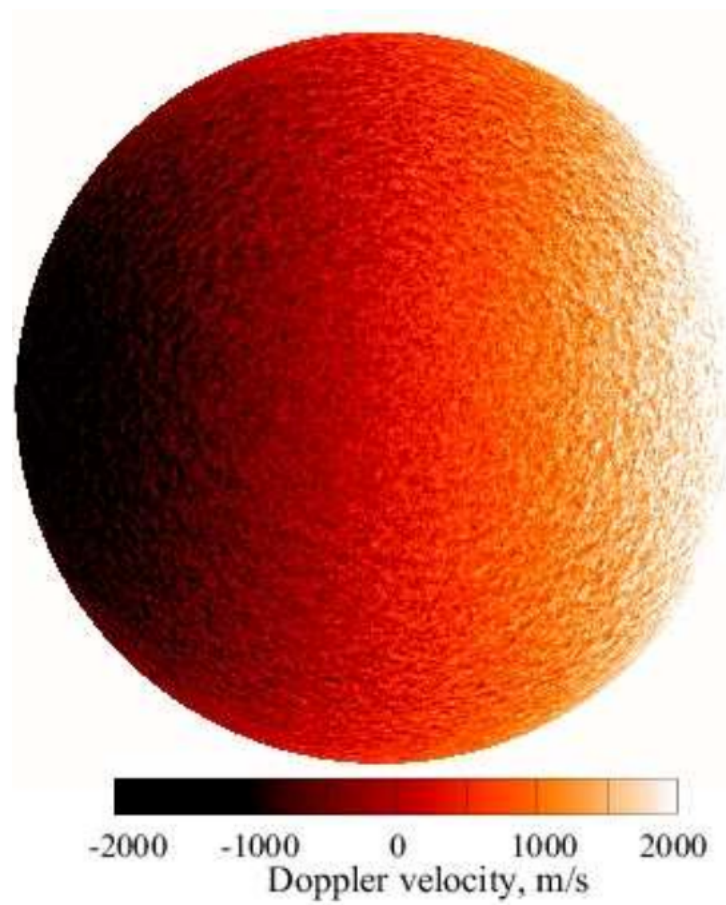


Fig. 1.1 Typical dopplergram image of sun showing line of sight velocity as the color field. Rotational profile of sun is clearly visible. Image taken by Michelson Doppler Imager aboard SOHO spacecraft. Image obtained from [\[1\]](#).

Chapter 2

Formalism

2.1 Standard Model and Frequency splittings

2.1.1 Background equation of motion

The standard solar model assumed in this work is that of a spherically symmetric, non-rotating, non-magnetic, adiabatic, isotropic, and static (SNRNMAIS). When equations of motion solved for displacement field $\boldsymbol{\xi}$ about the static equilibrium configuration, the SNRNMAIS model is found to admit wavelike solutions in displacement obeying the following differential equation in temporal frequency domain.

$$\mathcal{L}_0 \boldsymbol{\xi} \equiv -\nabla(\rho c^2 \nabla \cdot \boldsymbol{\xi} - \rho g \boldsymbol{\xi} \cdot \hat{\mathbf{e}}_r) - g \hat{\mathbf{e}}_r \nabla \cdot (\rho \boldsymbol{\xi}) = \rho \omega^2 \boldsymbol{\xi} \quad (2.1)$$

where ω denotes the temporal frequency of the oscillation, $c(r)$ is the sound speed profile, $-g(r)\hat{\mathbf{e}}_r$ is the gravitational field, $\rho(r)$ is mass density and $\hat{\mathbf{e}}_r$ is the radial unit vector. For all ensuing calculations and derivations we write equation (2.1) in the form $\mathcal{L}_0 \boldsymbol{\xi} = \rho \omega^2 \boldsymbol{\xi}$ which is to be understood as an eigenvalue equation with the eigenvalue ω^2 . It can be shown that the unperturbed wave operator \mathcal{L}_0 is self-adjoint [4]. Flow fields, rotations, asphericities, anisotropies and non-radial variations in c, g, ρ can be captured as perturbation terms in equation (2.1). Although for the purpose of this study, we shall restrict ourselves to perturbations induced via presence of an axisymmetric flow (differential rotation) and global scale magnetic fields only.

Since the operator \mathcal{L}_0 is self-adjoint, it has a complete set of eigenfunctions and corresponding quantised set of eigenfrequencies. These eigenfunctions and corresponding eigenfrequencies are called *normal modes* and *resonant frequencies* respectively. After decomposing the displacement field $\boldsymbol{\xi}$ into vector spherical harmonics it can be shown that eigenfunctions are characterised by three quantum numbers known as the radial order n , harmonic degree l and azimuthal order m . The eigenvalue equation is then given by

$$\mathcal{L}_0 \boldsymbol{\xi}_{nlm} = \rho \omega_{nl}^2 \boldsymbol{\xi}_{nlm} \quad (2.2)$$

where ω_{nl} is the eigenfrequency of the mode ξ_{nlm} . As consequence of the spherical symmetry, the eigenfrequencies ω_{nlm} are independent of the azimuthal quantum number m and are thus given by ω_{nl} . When any internal structure parameter such as convective flow, differential rotation, magnetic fields etc is introduced in the description of the system, they can be treated as a departure from the SNRNMAIS model. This leads to a lifting in the degeneracy in mode frequencies ω_{nl} . These frequency splitting can be calculated via a perturbative analysis of the \mathcal{L}_0 operator and its spectrum. The *forward problem* in global helioseismology is to find the relation between these split frequencies and these internal parameters. The essential idea of the *inverse problem* is to systematically deduce these internal structure parameters from frequency splittings of solar acoustic resonant modes.

2.1.2 Form of eigenfunction

A vector spherical harmonic decomposition of a vector field $\mathbf{A}(\mathbf{r})$ is given as

$$\mathbf{A}(\mathbf{r}) = \sum_{lm} [U_{lm}(r)Y_l^m \hat{\mathbf{e}}_r + V_{lm}(r)\nabla_1 Y_l^m + W_{lm}(r)\hat{\mathbf{e}}_r \times \nabla_1 Y_l^m] \quad (2.3)$$

where $\mathbf{r} = (r, \theta, \phi)$ in spherical polar coordinate system with basis vectors $(\hat{\mathbf{e}}_r, \hat{\mathbf{e}}_\theta, \hat{\mathbf{e}}_\phi)$, $\nabla_1 \equiv (\hat{\mathbf{e}}_\theta \partial_\theta + \hat{\mathbf{e}}_\phi \frac{1}{\sin \theta} \partial_\phi)$. Here, the first two parts involving U_{lm} and V_{lm} constitute the *spheroidal* (or poloidal) component and the last part is constitutes the *toroidal* component. Note that the spheroidal component has zero curl (irrotational) and the toroidal part has zero divergence (solenoidal).

Since the sun is essentially a fluid system, it is capable of offering restoring stress in response (and in proportion) to *shear strain rate* (shearing viscosity) but no restoring stress in response to *shear strain*, unlike the earth. This leads to the solar eigenfunctions lacking a toroidal component $(\hat{\mathbf{e}}_r \times \nabla_1 Y_l^m)$ [2]. Hence, they have the form

$$\xi_{nlm}(\mathbf{r}) = U_{nl}(r)Y_l^m(\theta, \phi)\hat{\mathbf{e}}_r + V_{nl}(r)\nabla_1 Y_l^m(\theta, \phi) \quad (2.4)$$

The entire set of $(2l + 1)$ degenerate SNRNMAIS eigenmodes having unperturbed frequency ω_{nl} is called ${}_nS_l$ where the S stands for ‘spheroidal’. This nomenclature borrows from the ‘spheroidal + toroidal’ decomposition of vector fields where the former is irrotational and the latter is solenoidal [5]. In geophysics literature, one also encounters toroidal modes ${}_nT_l$ [6].

We work with normalised eigenfunctions ξ_k with the spherically symmetric background density $\rho(r)$ as the weight factor, which satisfy the orthonormality condition:

$$(\xi_{k'} | \rho \xi_k) = \delta_{n'n} \delta_{l'l} \delta_{m'm} \quad (2.5)$$

where $k = (n, l, m)$, and the inner product $(|)$ stands for $(\Phi | \Psi) \equiv \int_{\odot} d^3\mathbf{r} \Phi^*(\mathbf{r}) \cdot \Psi(\mathbf{r})$.

2.2 Quasi Degenerate Perturbation Theory

Quasi-degenerate perturbation theory (QDPT) requires us to account for mixing of modes which lie in a small neighbourhood on the frequency spectrum, and hence satisfy the quasi-degenerate condition

$$|\omega_k^2 - \omega_{ref}^2| < \tau^2 \quad (2.6)$$

where ω_{ref} is some reference frequency defining the centre of the frequency interval. At the end of the section we'll demonstrate that degenerate perturbation theory (DPT) is a special case of QDPT.

Consider a set of multiplets ${}_n S_l$ lying close enough on the frequency spectrum to satisfy the quasi-degenerate condition (2.6). Let the entire space spanned by these functions be called \mathcal{K} . Then, as a perturbation $\mathcal{L} \rightarrow \mathcal{L} + \delta\mathcal{L}$ is introduced, the following changes are also introduced into the system

$$\xi_k \rightarrow \tilde{\xi} + \delta\tilde{\xi} \quad (2.7)$$

$$\omega_k^2 \rightarrow \omega_{ref}^2 + \delta(\omega^2) \quad (2.8)$$

where $\tilde{\xi}$ is a linear combination of all the modes in \mathcal{K} given by $\tilde{\xi} = \sum_{k \in \mathcal{K}} c_k \xi_k$ and $\delta\tilde{\xi}$ is a correction vector lying in \mathcal{K}' which is the orthogonal space of \mathcal{K} . Now, the new perturbed equation of motion is written as

$$(\mathcal{L} + \delta\mathcal{L}) (\tilde{\xi} + \delta\tilde{\xi}) = \rho (\omega_{ref}^2 + \delta(\omega^2)) (\tilde{\xi} + \delta\tilde{\xi}) \quad (2.9)$$

Expanding above equation and taking an inner product on both sides with ξ_k gives

$$\sum_{k' \in \mathcal{K}} Z_{kk'} c_{k'} = \delta(\omega^2) c_k \quad (2.10)$$

where $Z_{k'k}$ is the supermatrix defined as

$$Z_{k'k} \equiv (\xi_{k'} | \delta\mathcal{L} \xi_k) - \delta_{k'k} (\omega_{ref}^2 - \omega_k^2) \quad (2.11)$$

We can see that the leading order correction in eigenfrequency is given by the eigenvalues to the supermatrix $Z_{k'k}$ in equation (2.10). We also find that $\tilde{\xi}$ can be recovered as its decomposition coefficients in \mathcal{K} space is described by the eigenvectors of the supermatrix.

Note: The quantity $(\xi_{k'} | \delta\mathcal{L} \xi_k)$ will be referred to as the coupling matrix $\Lambda_{k'k}$ throughout this work to reduce notational burden.

Finally, as a corollary of the theory developed above, let us consider the case of \mathcal{K} consisting of modes that are all degenerate with frequency ω_0 . In this case, setting $\omega_{ref} = \omega_0$, we see that $Z_{k'k}$ reduces to $\Lambda_{k'k}$. Now the leading order corrections to eigenfrequency and eigenfunction are described by eigenvalue and eigenvectors of $\Lambda_{k'k}$; this is known as degenerate perturbation theory (DPT). A more detailed version of this analysis can be found in [5].

2.3 Representation of Splitting Data

Since each multiplet ${}_nS_l$ contains $2l + 1$ singlet modes, it is tedious to give the degree of splitting in the mode by exact value of each split frequency ω_{nlm} by itself. Therefore in helioseismology, splitting data is represented by numbers called splitting coefficients which describe the decomposition of $\delta\omega_{nlm} = \omega_{nlm} - \omega_{nl}$ in terms of some basis function over m as follows

$$\omega_{nlm} = \omega_{nl} + \sum_{j=0}^{j_{max}} a_j^{nl} \mathcal{P}_j^{(l)}(m) \quad (2.12)$$

where $\mathcal{P}_j^{(l)}(m)$ with $j \in \{0, 1, 2, \dots, j_{max}\}$ represents a $j_{max} + 1$ dimensional orthogonal basis function of polynomials on the discrete space of m 's which run from $-l$ to l . Since, there are $2l + 1$ points in this discrete domain, the (vector) space spanned by all functions on this domain is $(2l + 1)$ dimensional, which in turn means j_{max} cannot exceed $2l$. In practice, a -coefficients are recorded till a j_{max} of 10 ([7] for instance). We will use, as a standard, the basis functions prescribed in [8] which are Gram-Schmidt orthogonalised polynomials of increasing degree starting with $\mathcal{P}_0^{(l)}(m) = l$. Given the normalisation condition mentioned above, and this starting condition, the polynomials become well defined. A recipe for obtaining these can be found in Appendix A of [9]. Some properties to note about these polynomials are

- $\mathcal{P}_j^{(l)}(m)$ is odd/even about $m = 0$ if j is odd/even respectively.
- $\mathcal{P}_j^{(l)}(m)$ has polynomial degree j in m .
- $\mathcal{P}_j^{(l)}(m)$ contains only odd/even powers of m if j is odd/even respectively.
- In limit $l \gg 1$, $\mathcal{P}_j^{(l)}(m) \approx lP_j(m/l)$, where P_j is Legendre polynomial of degree j .

Once we have the splitting data ω_{nlm} , one can easily compute the a -coefficients multiplying both sides of Eq.(2.12) by $\mathcal{P}_k^{(l)}(m)$, summing over all m , and finally using the orthogonality condition

$$\sum_{m=-l}^l \mathcal{P}_j^{(l)}(m) \mathcal{P}_k^{(l)}(m) = \delta_{jk} \sum_{m=-l}^l \left(\mathcal{P}_j^{(l)}(m) \right)^2$$

as

$$a_j^{nl} = \sum_{m=-l}^l \delta\omega_{nlm} \mathcal{P}_j^{(l)}(m) / \sum_{m=-l}^l \left(\mathcal{P}_j^{(l)}(m) \right)^2 \quad (2.13)$$

Note that even though scaled Legendre polynomials $lP_j(m/l)$ are not perfectly orthogonal on a discretised domain (under the inner product $(A|B) \equiv \sum_{m=-l}^l A^*(m)B(m)$), they are still linearly independent. However their use should be avoided as a basis to represent splitting data because value of a -coefficients will change slightly depending on j_{max} , i.e. how many a -coefficients are being fitted to the data; this occurs due to

2.3 Representation of Splitting Data

non-zero inner product between different basis functions. An orthogonal basis like $\mathcal{P}_j^{(l)}$ solves this issue by making a_j values independent of j_{max} .

Thus, when ‘ a -coefficients’ are referred to in this text henceforth, it shall be understood that the underlying basis functions are given by $\{\mathcal{P}_j^{(l)} : j \in \{0, 1, \dots, j_{max}\}\}$. The first six $\mathcal{P}^{(l)}$ ’s are given below.

$$\mathcal{P}_0^{(l)}(m) = l \quad (2.14)$$

$$\mathcal{P}_1^{(l)}(m) = m \quad (2.15)$$

$$\mathcal{P}_2^{(l)}(m) = \frac{3m^2 - l(l+1)}{2l-1} \quad (2.16)$$

$$\mathcal{P}_3^{(l)}(m) = \frac{5m^3 - 3ml^2}{2l^2} \quad (2.17)$$

$$\mathcal{P}_4^{(l)}(m) = \frac{105m^4 - 90m^2l^2 + (9l^4 - 12l^3 - 14l^2 + 7l)}{(2l-1)(12l^2-7)} \quad (2.18)$$

$$\mathcal{P}_5^{(l)}(m) = \frac{63m^5 - 70m^3l^2 + 15ml^4}{8l^4} \quad (2.19)$$

Figure (2.1) shows that $\mathcal{P}_j^{(l)}(m)$ bear close resemblance with scaled Legendre polynomials $lP(m/l)$.

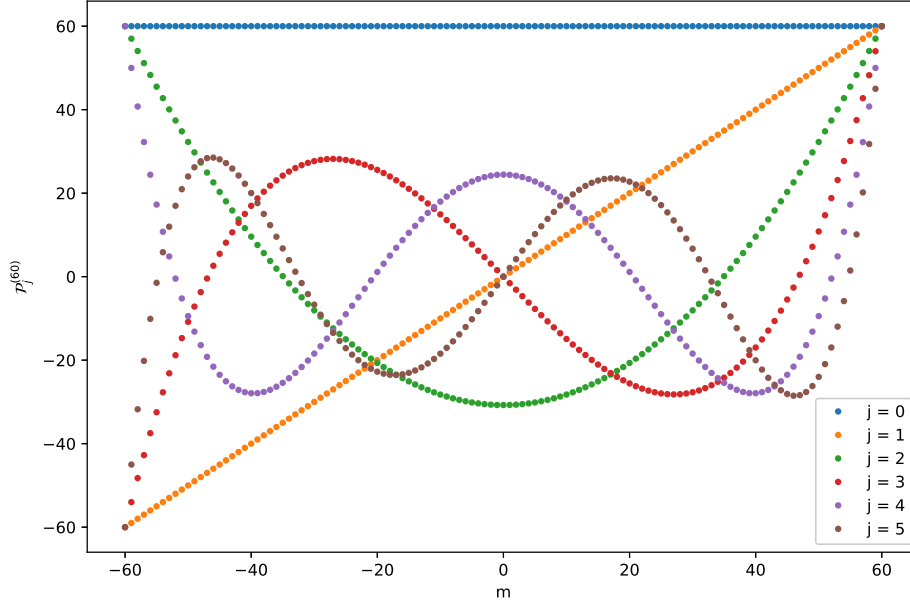


Fig. 2.1 Orthogonal basis functions $\mathcal{P}_j^{(l)}$ upto $j = 5$ for $l = 60$.

Chapter 3

The Rotating Sun

3.1 Differential Rotation

The sun is known to rotate differentially, unlike the earth. This means that angular rate of rotation of a point in the sun about its spin axis is depends on depth and latitude, $\Omega = \Omega(r, \theta)$. Splitting of p-mode¹ frequencies due to differential rotation is well understood and has a long history of inversion analysis [8, 5, 10]. This Ω is generally taken to be symmetric about the equatorial plane [8].

As a result of Alfven's freezing theorem², differential rotation is responsible for winding the solar magnetic field around its spin axis in an axisymmetric fashion. Thus we'll be investigating the effects of an axis symmetric magnetic field on the spectrum in this work, although the method we develop can very well accommodate non-axisymmetric fields too.

3.2 Detection from frequency spectrum

Because of axis symmetry of differential rotation, the flow profile is given as,

$$\mathbf{v}_{rot} = \sum_{s=1,3,5,\dots}^{\infty} -w_s^0(r) \partial_{\theta} Y_s^0 \hat{e}_{\phi} \quad (3.1)$$

Note that w_1^0 is responsible for shell like (pure) rotation as it couples with $\partial_{\theta} Y_1^0 \sim \sin \theta$. Hence w_3^0 onwards components of flow are responsible for the differential part of the rotation. The fact that the azimuthal index for the \mathbf{v}_{rot} profile is 0 means that it has no azimuthal dependence. Finding frequency splittings due to differential rotation is a problem in DPT or QDPT depending on whether we're using the isolated multiplet approximation or not. The isolated multiplet approximation is the assumption that there

¹pressure waves are also called p-modes

²Alfven's freezing theorem states that in a perfectly conducting plasma, magnetic flux through *every* surface is conserved as it gets dragged along with the ambient flow. See [4] for proof. This theorem implies that magnetic field lines are *frozen* in the plasma as it flows.

exists negligible cross coupling between different ${}_nS_l$ modes. Below we outline the QDPT approach to the problem because when applied to a single multiplet ${}_nS_l$ it reduces to the DPT approach. It has been argued via analysis differential rotation coupling of ${}_nS_1$ and ${}_nS_3$ multiplets that eigenfrequency correction to DPT via QDPT from cross coupling between these two is negligible ($\sim 1\mu Hz$) [5]. We'll show in Chapter 5 (figure 5.1) that for $l \sim 100$ modes, a frequency corrections of upto $600nHz$ frequencies are obtained when QDPT is used.

3.2.1 QDPT Analysis

The pertubation operator $\delta\mathcal{L}^v$ for a differential rotaional flow is given by

$$\delta\mathcal{L}^v = -2i\omega\rho\mathbf{v}_{rot} \cdot \nabla \quad (3.2)$$

where ω is the reference frequency in the problem, and ρ is the static background density profile [8]. The supermatrix element $Z_{k'k}$ for a pertubation $\delta\mathcal{L}^v$ is given by

$$Z_{k'k} = \Lambda_{k'k}^v - \delta_{k'k}(\omega_{ref}^2 - \omega_k^2) \quad (3.3)$$

where Λ^v is the coupling matrix element $\Lambda^v = (\xi_{k'}|\delta\mathcal{L}^v\xi_k)$. Coupling matrix element is given by

$$\Lambda_{k'k}^v = 8\pi\omega_{ref}\gamma_{l'}\gamma_l \sum_{s=1,3,5,\dots} \gamma_s \begin{pmatrix} l' & s & l \\ -m & 0 & m \end{pmatrix} \int_{\odot} dr r^2 w_s^0(r) T_s(r) \quad (3.4)$$

where the sensitivity kernel T_s is given by

$$T_s(r) = (1 - (-1)^{s+l+l'})\Omega_{l'}^0\Omega_l^0 \begin{pmatrix} l' & s & l \\ -1 & 0 & 1 \end{pmatrix} r^{-1} \left(U'V + V'U - U'U \right. \\ \left. - \frac{1}{2} (l'(l'+1) + l(l+1) - s(s+1)V'V) \right) \quad (3.5)$$

where the rounded brackets represent Wigner 3j symbols [8], and γ_l and Ω_l^N are constants defined in Appendix A.2.

3.2.2 Selecion rules in mode coupling

This matrix element enforces the following selection rules for inter-mode interaction which derive from the properties of Wigner 3j symbols [5].

1. $m' = m$
2. $l' + l + s = \text{odd}$
3. $|l' - l| \leq s \leq l' + l$

It should be noted here that even though only sum over odd s is considered, the expression for T_s is general and holds for all s . This has been verified independently using the

Mathematica packaged developed for the sake of this work [11]. Hence, as far as self coupling is concerned ($l' = l$), T_s vanishes for even s . This means that even if $\Omega(\theta, \phi)$ had a component which is antisymmetric about the equatorial plane, DPT analysis would not reveal any signature of that in the frequency splittings.

Form of supermatrix $Z_{k'k}$

It is clear from selection rule (1) in 3.2.2 that $Z_{k'k}$ is going to be a sparse matrix consisting of a diagonal and a number of sub-diagonals (proportional to number of multiplets being considered). Also, as s is always odd, $l - l'$ has to be even for non-zero coupling as consequence of selection rule (2). This influences our choice of modes whose inter-coupling will be studied hereafter. Figure (3.1) is a visual representation of a typical supermatrix consisting of three multiplets. The logarithm scale demonstrates the order of magnitude difference between self-coupling (main diagonal elements), and cross-coupling (subdiagonal elements). Also notice that largest elements (yellow) are in the first and third section in the main diagonal. These are large because these frequencies are placed away from ω_{ref} which is taken to be mean of the three mode frequencies. The relative weakness of the sub-diagonal terms compared to the main-diagonals is because $l - l' \geq 2$ forces $s \geq 2$ which makes the largest component of differential rotation, i.e. w_1^0 , unable to couple these modes; w_3^0 and w_5^0 are one and two orders of magnitude smaller than w_1^0 respectively.

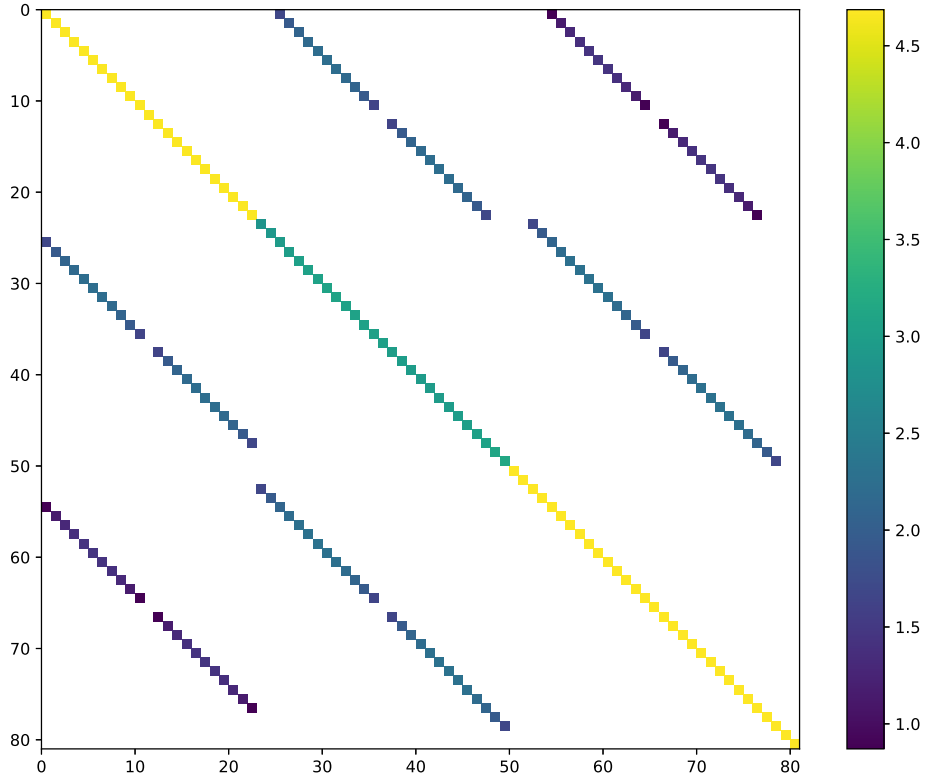


Fig. 3.1 Visualisation of $\log_{10}|Z_{k'k}|$ in μHz^2 for the multiplets ${}_0S_{11}$, ${}_0S_{13}$, and ${}_0S_{15}$ with frequencies $603.69\mu Hz$, $641.84\mu Hz$, and $677.55\mu Hz$ respectively. Numbers on the X and Y axes represent cumulative m of all three multiplets. White spaces correspond to 0 value.

Chapter 4

Internal Magnetic Fields

4.1 Solar Magnetic Field

It is well known through the observation of much surface solar phenomenon like active regions, solar flares, coronal mass ejections etc, that the sun has in its interior, often highly localised, significant magnetic fields. The source of this magnetic field is theorised to be a primordial current which started a dynamo process that is kept going at the expense of continuous dissipation of energy from the solar bulk. It is also widely believed however that mean magnetic field throughout the solar bulk is fairly weak. This chapter is devoted to finding a method to observe signature of this magnetic field in the p-mode frequency spectrum.

Most of high intensity magnetic activity is limited to the solar surface. The tachocline is believed to contain toroidal fields as high as 10^5G . outside the tachocline the magnetic field is believed to be mostly dipolar such that mean surface magnetic field is about 10G . Very strong time varying local magnetic fields apart from these are also known to exist near the surface, but detection of such time dependent fields is outside the scope of this work; here we shall only investigate the effects of steady fields.

4.2 Equation of Motion

In the presence of background magnetic field \mathbf{B} , the equation of motion is governed by the new operator $\mathcal{L} \rightarrow \mathcal{L} + \delta\mathcal{L}^B$, where $\delta\mathcal{L}^B$ is established in [12] as below.

$$\begin{aligned} \delta\mathcal{L}^B \boldsymbol{\xi} = & \frac{-1}{4\pi} \boldsymbol{\nabla} \cdot [\mathbf{B} \mathbf{B} \cdot \boldsymbol{\nabla} \boldsymbol{\xi} + \mathbf{B} \cdot \boldsymbol{\nabla} \boldsymbol{\xi} \mathbf{B} - 2\mathbf{B} \mathbf{B} \boldsymbol{\nabla} \cdot \boldsymbol{\xi} - (\boldsymbol{\xi} \cdot \boldsymbol{\nabla} \mathbf{B}) \mathbf{B} - \mathbf{B} (\boldsymbol{\xi} \cdot \boldsymbol{\nabla} \mathbf{B}) \\ & + B^2 \boldsymbol{\nabla} \cdot \boldsymbol{\xi} \mathbf{I} - \mathbf{B} \mathbf{B} : \boldsymbol{\nabla} \boldsymbol{\xi} \mathbf{I} + \boldsymbol{\xi} \cdot \boldsymbol{\nabla} \frac{B^2}{2} \mathbf{I}] \end{aligned} \quad (4.1)$$

where the $:$ stands for contraction of two second rank tensors ($\mathbf{P} : \mathbf{Q} \equiv P_{ij} Q_{ji}$).

Note that in above expression \mathbf{B} only appears in the second order. [4] contains a detailed derivation of this and a proof of self adjointness for $\delta\mathcal{L}^B$.

This expression can be put in a more convenient form involving the Lorentz stress tensor $\mathcal{H} \equiv \mathbf{B} \mathbf{B}$ as

$$\delta \mathcal{L}^B \xi = \frac{-1}{4\pi} \nabla \cdot [\mathcal{H} \cdot \nabla \xi + (\nabla \xi)^T \cdot \mathcal{H} - 2\mathcal{H} \nabla \cdot \xi - \xi \cdot \nabla \mathcal{H} + \mathcal{H} : I \nabla \cdot \xi I - \mathcal{H} : \nabla \xi I + \xi \cdot \nabla \left(\frac{\mathcal{H} : I}{2} \right) I] \quad (4.2)$$

4.3 Coupling Matrix

4.3.1 Lorentz Stress components

The process of taking integrals over a sphere becomes simplified if we're operating in the Generalised Spherical Harmonics formalism. In this formalism (Appendix A), magnetic field and Lorentz stress are decomposed as

$$\mathbf{B} = \sum_{st} \sum_{\alpha} B_{st}^{\alpha}(r) Y_{st}^{\alpha}(\theta, \phi) \hat{e}_{\alpha}$$

$$\mathcal{H} = \sum_{st} \sum_{\mu\nu} h_{st}^{\mu\nu}(r) Y_{st}^{\mu+\nu}(\theta, \phi) \hat{e}_{\mu} \hat{e}_{\nu}$$

where the generalised spherical harmonic (GSH) coordinate indices given by Greek symbols run from -1 to $+1$. Equation (4.11) relates the components of \mathcal{H} to \mathbf{B} . \mathcal{H} by construction satisfies the symmetry property $h_{st}^{\mu\nu} = h_{st}^{\nu\mu}$ ($\because \mathcal{H} = \mathbf{B} \mathbf{B}$), and $(h_{st}^{\mu\nu})^* = (-1)^t h_{st}^{\bar{\mu}\bar{\nu}}$, where overbars represent negatives, follows from its realness condition.

4.3.2 Sensitivity Kernels

Coupling matrix element is given as on integral transform over \mathcal{H} as

$$\Lambda_{k'k}^B = (\xi_{k'} | \delta \mathcal{L}^B \xi_k) = \int_0^{R_{\odot}} dr r^2 \sum_{\substack{st \\ \mu\nu}} \mathcal{B}_{st}^{\mu\nu}(r) h_{st}^{\mu\nu}(r) \quad (4.3)$$

where $\mathcal{B}_{st}^{\mu\nu}$ are the eigenfunction dependent magnetic sensitivity kernels. Prescription for evaluating these kernels and the explicit expressions can be found in [12]. It should be noted however that the coupling integral $(\xi_{k'} | \delta \mathcal{L}^B \xi_k)$ can be reduced to the radial integral form obtained in (4.3) contains no boundary terms. It is indeed the case that the magnetic field is assumed to vanish at the surface in this analysis. Relaxing this assumption will introduce boundary terms which involve integrals only over the solar surface. Since $h_{st}^{\mu\nu}$ is symmetric in interchange of μ and ν , we may ascribe the same symmetry to $\mathcal{B}_{st}^{\mu\nu}$ too without any loss in generality.

Using the Mathematica package developed for this work [11] which automates manipulation of tensor spherical harmonics via the method of GSHs, the following forms of the kernels were found

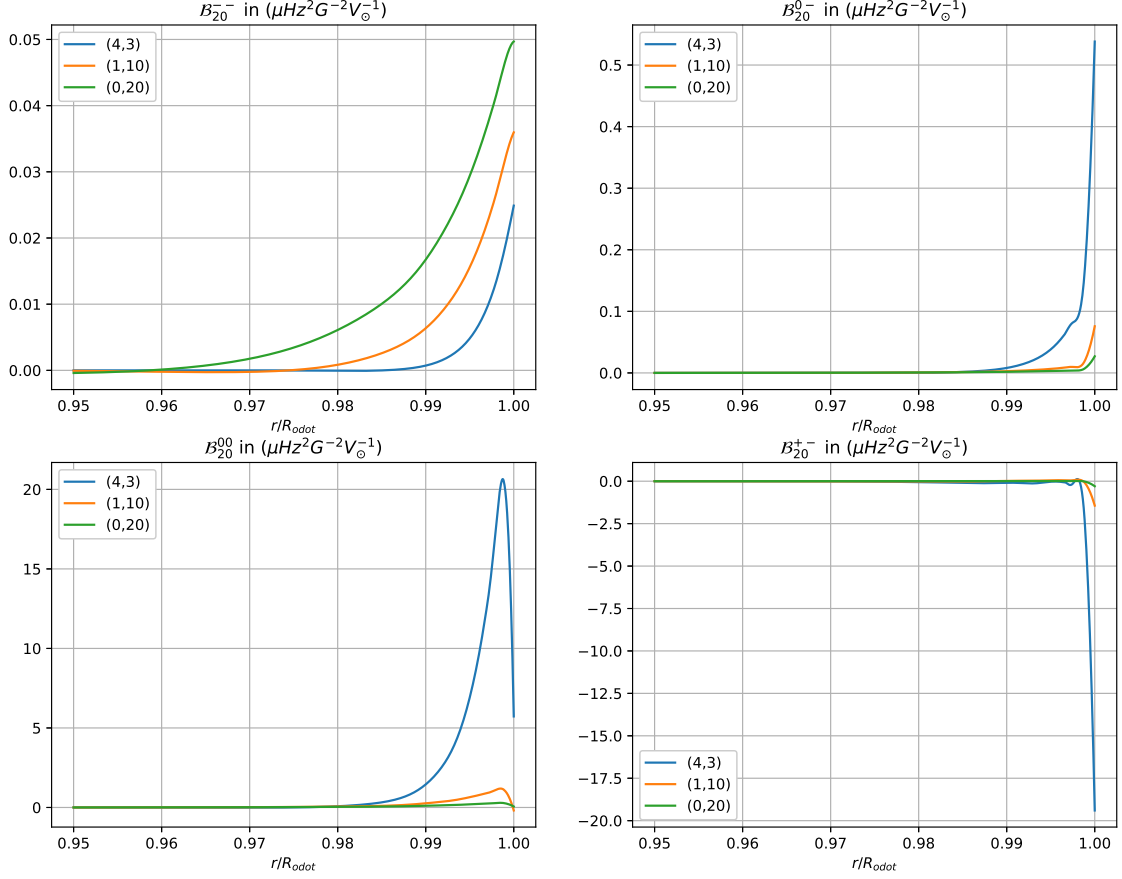
$$\begin{aligned} \mathcal{B}_{st}^{--} = & \frac{(-1)^{m'+1}}{r^2} \gamma_l \gamma_{l'} \gamma_s \begin{pmatrix} l' & s & l \\ -m' & t & m \end{pmatrix} \left\{ \begin{pmatrix} l' & s & l \\ 1 & -2 & 1 \end{pmatrix} \Omega_l^0 \Omega_{l'}^0 \left[(U + \Omega_{l'}^2 V) V' - U U' - r V \dot{V}' \right] \right. \\ & + \begin{pmatrix} l' & s & l \\ 2 & -2 & 0 \end{pmatrix} \Omega_{l'}^0 \Omega_{l'}^2 \left[(U + r \dot{U}) V' - r U \dot{V}' \right] + \begin{pmatrix} l' & s & l \\ 0 & -2 & 2 \end{pmatrix} \Omega_l^0 \Omega_l^2 r V \dot{U}' \\ & \left. + \begin{pmatrix} l' & s & l \\ 3 & -2 & -1 \end{pmatrix} \Omega_l^0 \Omega_{l'}^0 \Omega_{l'}^2 \Omega_{l'}^3 V V' \right\} \end{aligned} \quad (4.4)$$

$$\begin{aligned} 2\mathcal{B}_{st}^{0-} = & \frac{(-1)^{m'}}{r^2} \gamma_l \gamma_{l'} \gamma_s \begin{pmatrix} l' & s & l \\ -m' & t & m \end{pmatrix} \left\{ \begin{pmatrix} l' & s & l \\ 0 & -1 & 1 \end{pmatrix} \Omega_l^0 \left[(2U + \Omega_{l'}^2 V) U' \right. \right. \\ & + \Omega_{l'}^0 \left[(-2UV' - VV' + rV\dot{V}') - r(U + V - r\dot{V}') \dot{U}' \right] \\ & - \begin{pmatrix} l' & s & l \\ 1 & -1 & 0 \end{pmatrix} \Omega_{l'}^0 \left[(-2U + \Omega_l^2 V) U' + \Omega_l^2 V (r\dot{V}' - V') \right. \\ & + U(2V' + r(\dot{U}' - 2\dot{V}' + r\ddot{V}')) \left. \right] + \begin{pmatrix} l' & s & l \\ -1 & -1 & 2 \end{pmatrix} \Omega_l^0 \Omega_{l'}^0 \Omega_l^2 V [U' - V' + r\dot{V}'] \\ & \left. + \begin{pmatrix} l' & s & l \\ 2 & -1 & -1 \end{pmatrix} \Omega_l^0 \Omega_{l'}^0 \Omega_{l'}^2 [V(U' - 3V' + r\dot{V}') + 2r\dot{V}V'] \right\} \end{aligned} \quad (4.5)$$

$$\begin{aligned} \mathcal{B}_{st}^{00} = & \frac{(-1)^{m'}}{2r^2} \gamma_l \gamma_{l'} \gamma_s \begin{pmatrix} l' & s & l \\ -m' & t & m \end{pmatrix} (1+p) \left\{ \frac{1}{2} \begin{pmatrix} l' & s & l \\ 0 & 0 & 0 \end{pmatrix} \left[(6U - 4\Omega_l^2 V - 2r\dot{U}) (U' - \Omega_{l'}^2 V') \right. \right. \\ & + 2\Omega_{l'}^2 rU\dot{V}' + r((-4U + 2\Omega_l^2 V + r\dot{U})) \dot{U}' + rU\ddot{U}' \\ & - \begin{pmatrix} l' & s & l \\ -1 & 0 & 1 \end{pmatrix} \Omega_{l'}^0 \Omega_l^0 [V(-4U' + 2(1 + \Omega_{l'}^2) V' + r(\dot{U}' - 2\dot{V}')) \\ & \left. \left. + 2r\dot{V}(U' - V' + r\dot{V}') \right] \right\} \end{aligned} \quad (4.6)$$

$$\begin{aligned} 2\mathcal{B}_{st}^{+-} = & \frac{(-1)^{m'}}{r^2} \gamma_l \gamma_{l'} \gamma_s \begin{pmatrix} l' & s & l \\ -m' & t & m \end{pmatrix} (1+p) \left\{ -2 \begin{pmatrix} l' & s & l \\ -2 & 0 & 2 \end{pmatrix} \Omega_l^0 \Omega_l^2 \Omega_{l'}^0 \Omega_{l'}^2 V V' \right. \\ & \left. + \begin{pmatrix} l' & s & l \\ -1 & 0 & 1 \end{pmatrix} \Omega_{l'}^0 \Omega_l^0 [-rV\dot{U}' + U(U' - V' + r\dot{V}')] + \begin{pmatrix} l' & s & l \\ 0 & 0 & 0 \end{pmatrix} r^2 [U\ddot{U}' - \dot{U}\dot{U}'] \right\} \end{aligned} \quad (4.7)$$

where $p \equiv (-1)^{l'+l+s}$, $U, V \equiv U_{nl}, V_{nl}$, and $U', V' \equiv U_{n'l'}, V_{n'l'}$.


 Fig. 4.1 Self coupling Kernels for the modes $4S_3$, $1S_{10}$, and $0S_{20}$.

Kernel components $\mathcal{B}_{st}^{\mu\nu}$ are found to have these following properties:

1. $\mathcal{B}_{st}^{\mu\nu} = \mathcal{B}_{st}^{\nu\mu}$ (by construction)
2. $\mathcal{B}_{st}^{--} = (-1)^{l+l'+s} \mathcal{B}_{st}^{++}$
3. $\mathcal{B}_{st}^{0-} = (-1)^{l+l'+s} \mathcal{B}_{st}^{+0}$
4. $\mathcal{B}_{st}^{00} = \mathcal{B}_{st}^{+-} = \mathcal{B}_{st}^{-+} = 0$ for odd $(l' + l + s)$

Figure (4.1) shows the four independent components of the sensitivity kernel under self coupling for some modes. It is clear from the plots that for all modes, sensitivity is mostly localised to the solar boundary. This effect is most striking for \mathcal{B}_{st}^{+-} across modes. This is an indirect consequence of the background density profile of the sun which falls almost exponentially fast with respect to radius towards the outer regions

of the sun. The low density near the boundary makes the eigenfunction peak distinctly near the boundary. However, as can be seen in equations (4.4) - (4.7), the kernels depend quadratically on U and V , which finally makes them peak at the boundary. This implies that most of the magnetic splitting caused is due to the fields near the surface and acts as limitation to imaging the interior magnetic field precisely via an inversion of frequency splitting data.

We can see that how it is ultimately the components of \mathcal{H} that couple with the sensitivity kernel; components of \mathbf{B} cannot be related to frequency splittings in a straightforward manner like equation (4.3). Hence, any procedure inverting splitting data will first determine the \mathcal{H} components. It remains unclear if the magnetic field can be recovered from just the knowledge of components of \mathcal{H} .

4.4 Synthetic Magnetic Field

Using some basic pieces of information about mean solar magnetic field as given in 4.1, we can posit the following form of a synthetic magnetic field which will be used for validating our routine of finding frequency splits. We give the following form of the magnetic field which is composed of an internal toroidal field concentrated at the core and the tachocline, and a dipolar field which extends from the tachocline to the surface.

4.4.1 Construction of \mathbf{B}

Using the identities $\nabla_1 Y_l^m = \Omega_l^0 (Y_{lm}^{-1} \hat{\mathbf{e}}_- + Y_{lm}^1 \hat{\mathbf{e}}_+)$, $\hat{\mathbf{e}}_r \times \nabla_1 Y_l^m = i\Omega_l^0 (Y_{lm}^{-1} \hat{\mathbf{e}}_- - Y_{lm}^1 \hat{\mathbf{e}}_+)$, and $Y_1^0(\theta, \phi) = \gamma_1 \cos \theta$ we see following things: (1) A toroidal field $\mathbf{B} = \alpha(r) \sin \theta \hat{\mathbf{e}}_\phi$ can be given as $B_{10} = i\alpha(r)/\gamma_1 (-1, 0, 1)$ with all other B_{st} components being 0, and (2) A dipolar field $\mathbf{B} = \beta(r)(2 \cos \theta \hat{\mathbf{e}}_r + \sin \theta \hat{\mathbf{e}}_\theta)$ with $\beta \propto r^{-3}$ can be given as $B_{10} = -\beta(r)/\gamma_1 (1, -2, 1)$ with all other B_{st} components being 0. Note that the row vector refers to the GSH coordinate index μ . This leads to the following final form of \mathbf{B}

$$B_{st}(r) = \begin{cases} -i\frac{\alpha(r)}{\gamma_1} \begin{pmatrix} 1 \\ 0 \\ -1 \end{pmatrix} - \frac{\beta(r)}{\gamma_1} \begin{pmatrix} b - r\dot{b} \\ -2b \\ b - r\dot{b} \end{pmatrix}, & \text{for } (s, t) = (1, 0) \\ 0, & \text{for } (s, t) \neq (1, 0) \end{cases} \quad (4.8)$$

where $b(r) = 1$ where field is perfectly dipolar. The term $r\dot{b}(r)$ appear as a consequence of fixing the divergence to zero and is only nonzero in the transition region where $b(r)$ goes from 0 to 1. It can be checked via using $\nabla \cdot \mathbf{B} = g_{\alpha\beta}(\nabla \mathbf{B})^{\alpha\beta}$ ([11] was used) that the two parts in (4.8) (toroidal and dipolar) satisfy the solenoidal condition independently. We plot the forms of the α , β , and b used in our frequency splitting calculations.

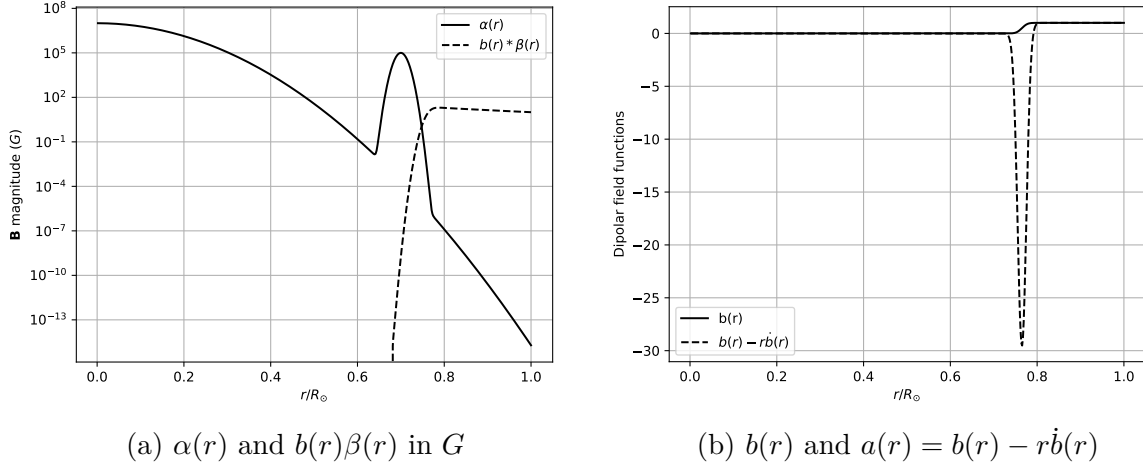


Fig. 4.2 $\alpha(r)$ is addition of two Gaussians centred at $r = 0$ with peak $10^7 G$ and at $r = 0.7R_\odot$ with peak $10^5 G$ respectively. b transitions smoothly from 0 to 1 as a sigmoid around $r = 0.7R_\odot$. $r = 0.7R_\odot$ mark is roughly where the tachocline is placed. Figure (4.2a) shows the poloidal (dipolar) field β starting to dominate over the toroidal field by atleast three orders of magnitude as r exceeds $\sim 0.8R_\odot$.

4.4.2 Construction of \mathcal{H}

After the form of \mathbf{B} has been ascertained, it is straightforward to derive components of \mathcal{H} via taking a tensor product. Decomposing either field in their GSH forms as in 4.3.1, and using orthonormality relation

$$\int d\Omega \left(Y_{l_1 m_1}^{n_1} \right)^* Y_{l_2 m_2}^{n_2} = \delta_{l_1 l_2} \delta_{m_1 m_2} \delta_{N_1 N_2} \quad (4.9)$$

and the triple integral result

$$\int d\Omega \left(Y_{l_1 m_1}^{N_1} \right)^* Y_{l_2 m_2}^{N_2} Y_{l_3 m_3}^{N_3} = (-1)^{m_1 + N_1} 4\pi \gamma_{l_1} \gamma_{l_2} \gamma_{l_3} \begin{pmatrix} l_1 & l_2 & l_3 \\ -m_1 & m_2 & m_3 \end{pmatrix} \begin{pmatrix} l_1 & l_2 & l_3 \\ -N_1 & N_2 & N_3 \end{pmatrix} \quad (4.10)$$

one can write

$$h_{st}^{\mu\nu} = \sum_{\substack{s_1 t_1 \\ s_2 t_2}} \langle Y_{st}^{\mu+\nu}, Y_{s_1 t_1}^\mu Y_{s_2 t_2}^\nu \rangle B_{s_1 t_1}^\mu B_{s_2 t_2}^\nu \quad (4.11)$$

Where $\langle Y_{l_1 m_1}^{N_1}, Y_{l_2 m_2}^{N_2} Y_{l_3 m_3}^{N_3} \rangle$ stands for the integral in equation (4.10). If \mathbf{B} has only $s = s_0$ and $t = t_0$ features, that is $\mathbf{B} = \sum_\alpha B_{s_0 t_0}^\alpha Y_{s_0 t_0}^\alpha \hat{\mathbf{e}}_\alpha$, components of \mathcal{H} are given by

$$h_{st}^{\mu\nu} = B_{s_0 t_0}^\mu B_{s_0 t_0}^\nu (-1)^{\mu+\nu+t} (2s_0 + 1) \gamma_s \begin{pmatrix} s_0 & s & s_0 \\ \mu & -(\mu+\nu) & \nu \end{pmatrix} \begin{pmatrix} s_0 & s & s_0 \\ t_0 & -t & t_0 \end{pmatrix} \quad (4.12)$$

Internal Magnetic Fields

For the axis symmetric magnetic field constructed in 4.4.1, we may set $s_0 = 1$ and $t_0 = 0$. Wigner 3j selection rules given in 3.2.2 dicte that \mathcal{H} can only have $s = 0, 1, 2$ and $t = 0$. Then we have the form

$$h_{s0}^{\mu\nu} = 3\gamma_s B_{10}^\mu B_{10}^\nu (-1)^{\mu+\nu} \begin{pmatrix} 1 & s & 1 \\ \mu & -(\mu+\nu) & \nu \end{pmatrix} \begin{pmatrix} 1 & s & 1 \\ 0 & 0 & 0 \end{pmatrix} \quad (4.13)$$

But we know that $\begin{pmatrix} 1 & s & 1 \\ 0 & 0 & 0 \end{pmatrix}$ vanishes for odd s . Thus we note here that \mathcal{H} has no $s = 1$ and has non-zero $s = 0$ components, which is different from how differential rotation couples modes. The $s = 0$ feature of the Lorentz stress tensor indicates a net shift from the unperturbed mode frequency ω_{nl} for a particular multiplet ${}_n S_l$ as this term couples with $\begin{pmatrix} l' & 0 & l \\ -m & 0 & m \end{pmatrix}$ which is independent of m .

Chapter 5

Results

5.1 Frequency Splittings due to Differential Rotation

In this treatment we show that while taking very closely spaced multiplets, the isolated multiplet condition breaks down and there is significant cross coupling across modes due to differential rotation alone. Because axis symmetry imposes the $m' = m$ selection rule, the supermatrix $Z_{k'k}$ of perturbation $\delta\mathcal{L}^v$ is a sparse matrix consisting of diagonals and subdiagonal as show in figure (3.1). As a case study, we choose to investigate the splitting coefficients of the mode ${}_0S_{77}$ as a result of cross coupling with its neighbouring modes which all lie withing an interval of $100\mu Hz$.

5.1.1 Splitting with pure rotation

We plot the split frequencies ${}_0S_{77}$ along with some neighbouring modes to contrast the results obtained from a QDPT and a DPT analysis.

a -coefficients obtained from the split is tabulated in table 5.2. a_1 's found from QDPT and DPT come out to be close to $440nHz$ which is corresponds to the 24 day rotational cycle of the sun. a_3 and a_5 are found to be in good agreement upto a tolerance of $1nHz$. However, the QDPT profile contains even a -coefficients of the order of $5nHz$. This leads to an even profile departure of the QDPT from DPT profile of the order of $600nHz$ in the frequency spectrum as shown in figure (5.1).

${}_nS_l$	${}_0S_{69}$	${}_0S_{71}$	${}_0S_{73}$	${}_0S_{75}$	${}_0S_{77}$	${}_0S_{79}$	${}_0S_{81}$	${}_0S_{83}$	${}_0S_{85}$
ω_{nl}	848.219	860.008	871.636	883.110	894.434	905.615	916.659	927.570	938.353

Table 5.1 Frequencies in μHz corresponding to all modes discussed in this chapter. These modes have been chosen to be in increasing order in frequency and satisfying the $\delta l = 2$ condition.

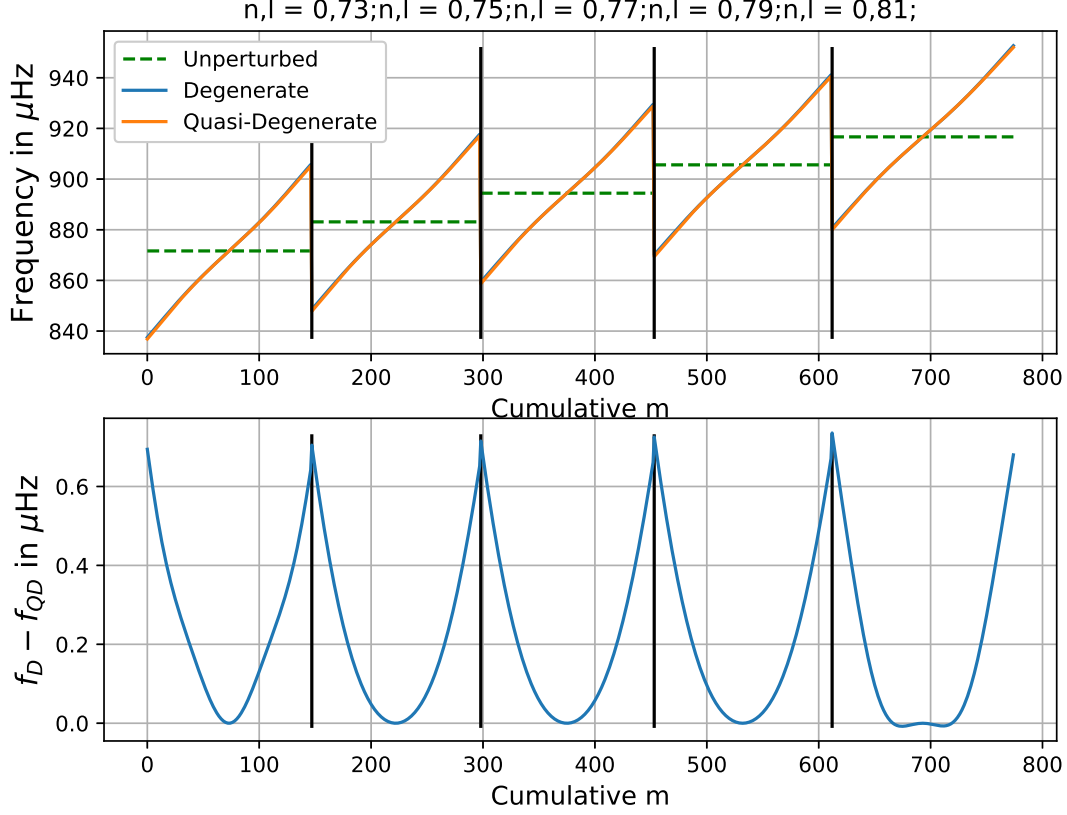


Fig. 5.1 DPT and QDPT splits with ${}_0S_{73}$, ${}_0S_{75}$, ${}_0S_{77}$, ${}_0S_{79}$, and ${}_0S_{81}$ which have frequencies $871.63\mu\text{Hz}$, $883.12\mu\text{Hz}$, $894.43\mu\text{Hz}$, $905.62\mu\text{Hz}$, and $916.66\mu\text{Hz}$ respectively. Top plot shows frequency splittings of the five modes and their unperturbed frequencies (green dashed). DPT and QDPT lie indiscernably. Bottom plot shows the departure of the DPT frequencies from the dpt frequencies.

5.1.2 Splitting with pure rotation removed

We see that the component $w_1^0(r)$ in the sun's rotational profile gives rise to a velocity field

$$\mathbf{v} = -w_1^0 \partial_\theta Y_1^0 \hat{\mathbf{e}}_\phi = \gamma_1 w_1^0 \sin \theta \hat{\mathbf{e}}_\phi$$

which corresponds to pure shell like rotation at each particular radius r . Taking $w_1^0 \rightarrow w_1^0 - \Omega_1 r / \gamma_1$ gives

$$\mathbf{v} = \gamma_1 w_1^0 \sin \theta \hat{\mathbf{e}}_\phi - \Omega_1 r \sin \theta \hat{\mathbf{e}}_\phi \quad (5.1)$$

and hence corresponds to slowing down each shell by an angular velocity Ω_1 about the spin axis. Thus, subtracting out $\Omega_1 r / \gamma_1$ from w_1^0 is equivalent to slowing down the pure rotational profile by angular velocity Ω_1 .

5.2 Splittings due to Lorentz Stresses

Mode	QDPT(nHz)	DPT(nHz)
a_0	-2.832	-
a_1	438.378	438.178
a_2	-5.876	-
a_3	22.149	22.005
a_4	-0.308	-
a_5	-4.925	-4.934
a_6	0.091	-
a_7	-0.002	-
a_8	-0.018	-
a_9	-	-
a_{10}	0.004	-

Table 5.2 Splitting coefficients for mode ${}_0S_{77}$ via QDPT and DPT analysis. Hyphens stand for values $< 0.001nHz$.

We see that after removing an pure rotation component equivalent to 440nHz from the w_1^0 rotational profile, we get the following splitting of frequencies for QDPT and DPT respectively as shown in figure (5.1). QDPT is performed taking 5 modes all lying in a band of width $100\mu Hz$.

QDPT vs DPT with increasing coupling modes

When QDPT is performed taking multiple neighbouring modes amongst the ones in table 5.1, a peculiar trend is found when comparing QDPT frequencies with their DPT counterparts for each singlet mode. The trend in figure (5.3) shows large deviations in QDPT splitting from DPT frequencies in modes placed at either extreme regardless of how many modes couple while QDPT-DPT departure in the inner modes stay the same. This hints at the large QDPT-DPT frequency differences obtained for the extremal modes being artefacts of the calculation and hence being unreliable. For reference henceforth, we only use QDPT frequencies of ${}_0S_{77}$ which remains relatively unchanged with respect to number of modes being considered.

5.2 Splittings due to Lorentz Stresses

For finding magnetic splitting of the frequency spectrum, we choose to go to the corotating frame ($440nHz$) to eliminate the dominant linear trend from the splitting profile and perform QDPT with the perturbation $\delta\mathcal{L}^B$ on a background spectrum which is already split by differential rotation. We are justified in doing this because eliminating a net rotational component is equivalent to a coordinate transformation [2]. In this treatment where the background profile is already split by differential rotation, our perturbation which couples different modes is $\delta\mathcal{L}^B$ (equation (4.1)). Background frequencies ω_{nlm} are

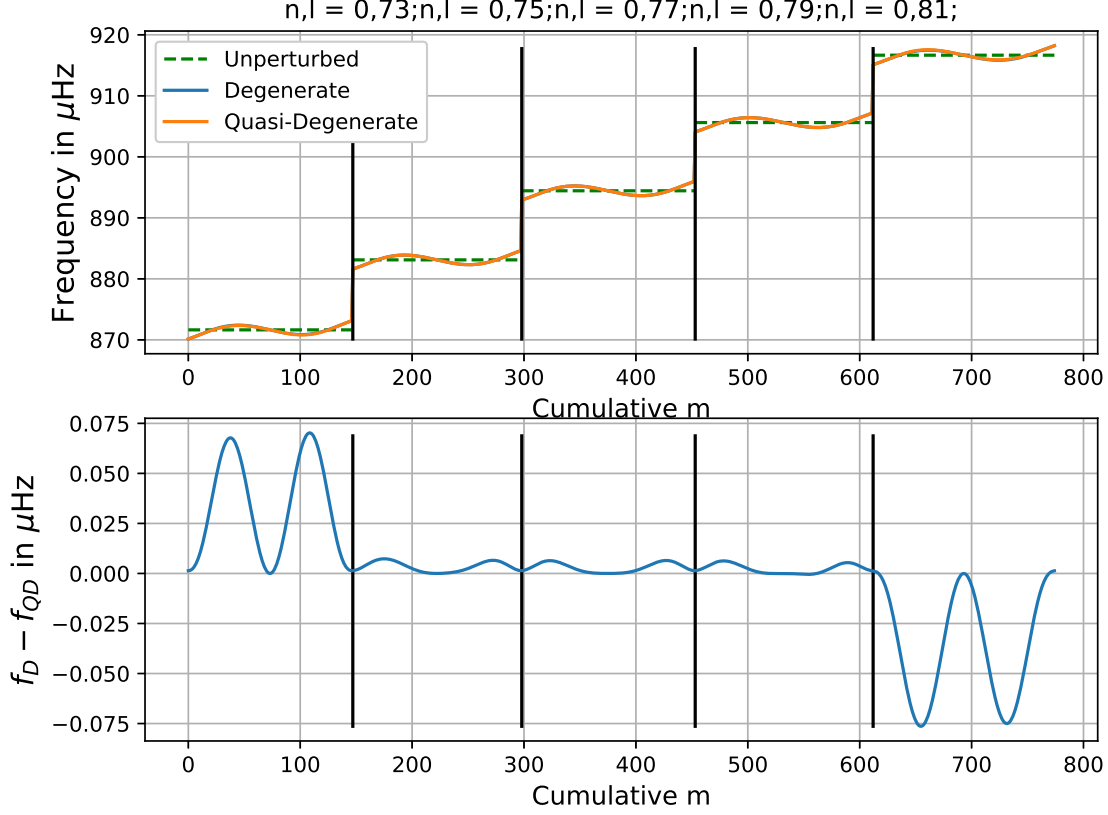


Fig. 5.2 DPT and QDPT rotational splits with pure rotational component equivalent to $440nHz$ removed from w_1^0 for modes ${}_0S_{73}$, ${}_0S_{75}$, ${}_0S_{77}$, ${}_0S_{79}$, and ${}_0S_{81}$ which have frequencies as shown in table (5.1). Top plot shows frequency splittings of the five modes and their unperturbed frequencies. Bottom plot shows the departure of the QDPT frequencies from the DPT frequencies.

obtained by performing DPT on degenerate modes ${}_nS_l$. We have chosen to perform DPT over QDPT for obtaining background ω_{nlm} 's to reduce computational burden because resultant frequencies differ by less than $10nHz$ (centre section of figure (5.2) corresponding to ${}_0S_{77}$) and odd a -coefficients are almost identical (table 5.2 shows the low relative error in odd a -coefficients).

The departure from the (rotating) background of the spectrum is shown in figure (5.4). The a -coefficients are listed in table 5.4. The table also contains the a -coefficients for magnetic splitting obtained from QDPT performed on a background with no rotation for comparison.

Mode	QDPT(nHz)	DPT(nHz)
a_0	-0.038	-
a_1	2.820	2.820
a_2	-0.030	-
a_3	22.005	22.005
a_4	0.071	-
a_5	-4.933	-4.934
a_6	-0.006	-
a_7	-	-
a_8	-0.018	-
a_9	-	-
a_{10}	0.004	-

Table 5.3 Splitting coefficients for the splitting of mode ${}_0S_{77}$ by QDPT and DPT analysis after removing pure rotational component equivalent to $440nHz$ from w_1^0 . Hyphens stand for values $< 0.001nHz$.

5.2.1 Detectability

the first two columns of table 5.4 show the effect of magnetic perturbation on even a -coefficients. While the non-magnetic rotating profile (obtained by DPT) contains no even a 's at all, the magnetic perturbation introduces $a_0 = 63pHz$ and $a_2 = -59pHz$. These pHz level a -coefficients are not detectable by current standards of precision in observation as minimum errors in observed coefficients lie in the $\sim 1nHz$ range [7].

5.3 Conclusion

We had started out with the goal of solving the forward problem of finding splittings in degenerate modes in the sun's acoustic frequency spectrum. This was aimed at the possibility of a future project to image the interior magnetic field by performing an inversion procedure on the observed splitting data by using the Lorentz stress sensitivity kernels obtained in 4.3.2. We constructed a magnetic field profile closely mimicking that of the sun to validate the kernels found. We found, by feeding our synthetic magnetic field in the sensitivity kernels and performing QDPT on nine neighbouring modes, that additional components of about $60pHz$ to a_0 and a_2 coefficients are being introduced to the splitting of the mode ${}_0S_{77}$. These changes to a -coefficients are smaller than errors in a -coefficients to have been recorded till now, and hence not detectable with current levels of available precision. In future, an increase in precision of recording these coefficients by two orders of magnitude will enable a realistic inversion of splitting data aimed at imaging Lorentz stress components in the interior of the sun.

Results

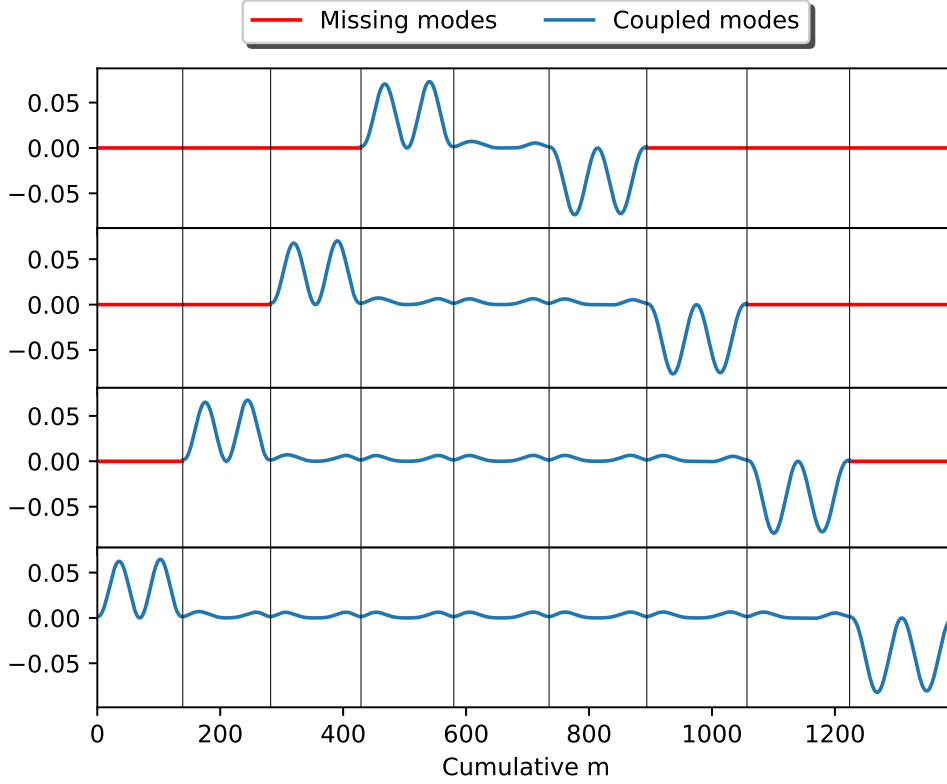


Fig. 5.3 (QDPT - DPT) deviation with differing number of neighbouring modes being allowed to couple via differential rotation with mean rotation removed. From top, ${}_0S_{77}$ is made to couple with two, four, six, and eight closest $\Delta l = 2$ neighbours (by frequency) as listed in table 5.1.

a_n	Magnetic QDPT (on rotating background)	Rotating Background (no magnetic field)	Magnetic DPT (on stationary background)
a_0	0.063	-	0.061
a_1	2.822	2.820	-
a_2	-0.059	-	-0.059
a_3	22.020	22.005	-
a_4	-	-	-
a_5	-4.937	-4.934	-

Table 5.4 Splitting coefficients in nHz for the magnetic splitting of mode ${}_0S_{77}$. First column is magnetic QDPT split on differentially rotating background (pure rotation removed) obtained by DPT. Second column in the background split for the first column. Third column is magnetic DPT performed on stationary sun. List has been truncated whence a 's vanish identically. Hyphens stand for values $< 0.001nHz$.

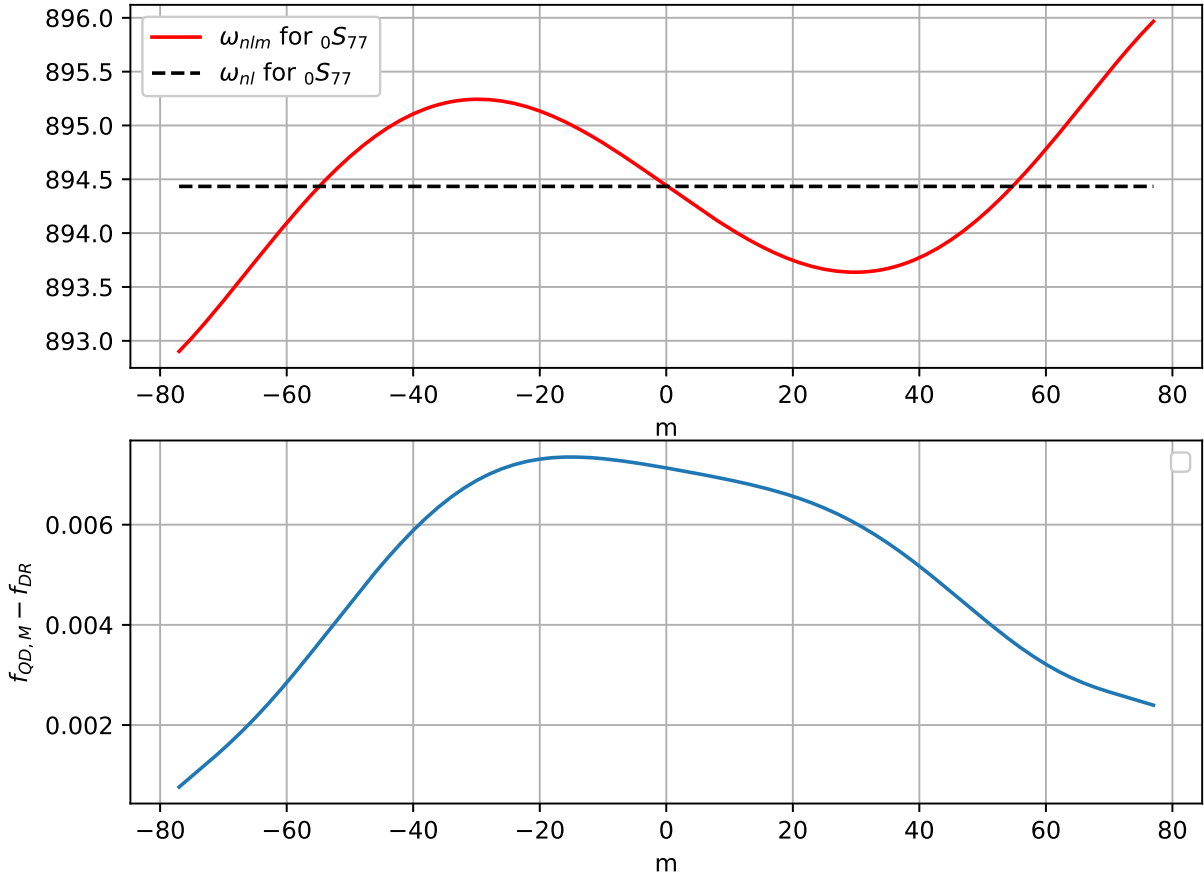


Fig. 5.4 Magnetic splitting profile of the mode ${}_0S_{77}$ obtained from QDPT containing all nine modes listed in table 5.1 on rotating background with $440nHz$ equivalent component removed from w_1^0 . Top shows the absolute frequency about the unperturbed baseline in μHz . Bottom shows the difference between the overall (rotation + magnetic field) and the background rotation profile obtained from DPT.

References

- [1] A. G. Kosovichev, *Advances in Global and Local Helioseismology: An Introductory Review*, pp. 3–84. Springer Berlin Heidelberg, Berlin, Heidelberg, 2011. 10.1007/978-3-642-19928-8_1.
- [2] J. Christensen-Dalsgaard, *Lecture Notes on Stellar Oscillations*. fifth ed., January, 2003.
- [3] L. Gizon and A. C. Birch, *Time-Distance Helioseismology: The Forward Problem for Random Distributed Sources*, *The Astrophysical Journal* **571** (2002) 966.
- [4] J. P. H. Goedbloed and S. Poedts, *Principles of Magnetohydrodynamics: with Applications to Laboratory and Astrophysical Plasmas*. Cambridge University Press, 2004, 10.2277/0521626072.
- [5] E. M. Lively and M. H. Ritzwoller, *The Effect of Global-Scale, Steady-State Convection and Elastic-Gravitational Asphericities on Helioseismic Oscillations*, *Philosophical Transactions of the Royal Society of London Series A* **339** (1992) 431.
- [6] F. A. Dahlen and J. Tromp, *Theoretical Global Seismology*. Princeton University Press, 1998.
- [7] J. Schou, “Index of / schou/anavw72z.” <http://quake.stanford.edu/~schou/anavw72z/?C=M;O=A>, 1999.
- [8] M. H. Ritzwoller and E. M. Lively, *A unified approach to the helioseismic forward and inverse problems of differential rotation*, *The Astrophysical Journal* **369** (1991) 557.
- [9] J. Schou, J. Christensen-Dalsgaard and M. Thompson, *On comparing helioseismic two-dimensional inversion methods*, *The Astrophysical Journal* **433** (1994) .
- [10] J. Schou, H. M. Antia, S. Basu, R. S. Bogart, R. I. Bush, S. M. Chitre et al., *Helioseismic Studies of Differential Rotation in the Solar Envelope by the Solar Oscillations Investigation Using the Michelson Doppler Imager*, *The Astrophysical Journal* **505** (1998) 390.
- [11] T. Chakraborty and S. B. Das, “Mathematica package for generalised spherical harmonic manipulation.” https://github.com/tuneerch/LStress_Mathematica, 2019.
- [12] S. M. Hanasoge, *Seismic sensitivity of normal-mode coupling to Lorentz stresses in the Sun*, *Monthly Notices of the Royal Astronomical Society* **470** (2017) 2780 [1705.09431].

- [13] R. A. Phinney and R. Burridge, *Representation of the Elastic - Gravitational Excitation of a Spherical Earth Model by Generalized Spherical Harmonics*, *Geophysical Journal International* **34** (1973) 451 [<http://oup.prod.sis.lan/gji/article-pdf/34/4/451/1912034/34-4-451.pdf>].
- [14] T. Chakraborty and S. B. Das, “Main repository for lorentz stress splitting calculation.” https://github.com/tuneerch/lorentz_stress_kernel, 2019.

Appendix A

Generalised Spherical Harmonics Formalism

A.1 Formalism

A general formalism to describe complex tensor fields on the surface of a 2-sphere is that of Generalised Spherical Harmonics. A generalisation of the spherical harmonic given by Y_{lm}^N , with an added index N , is used to decompose tensor fields of arbitrary rank [13]. It reduces to the spherical harmonic when $N = 0$.

$$Y_{lm}^0(\theta, \phi) = Y_l^m(\theta, \phi) \quad (\text{A.1})$$

These functions couple with the GSH unit vectors given by

$$\hat{e}_- = \frac{1}{\sqrt{2}}(\hat{e}_\theta - i\hat{e}_\phi), \quad \hat{e}_0 = \hat{e}_r, \quad \hat{e}_+ = -\frac{1}{\sqrt{2}}(\hat{e}_\theta + i\hat{e}_\phi) \quad (\text{A.2})$$

to form tensor spherical harmonics

$$\mathbf{Y}_{lm}^N \equiv Y_{lm}^N \hat{e}_{\alpha_1} \hat{e}_{\alpha_2} \dots \hat{e}_{\alpha_q} \quad (\text{A.3})$$

where $\alpha_1 + \alpha_2 + \dots + \alpha_q = N$. These tensor functions by construction are eigenfunctions of the total angular momentum operator $\hat{\mathbf{J}} = \hat{\mathbf{L}} + \hat{\mathbf{S}}$, where the first part $\hat{\mathbf{L}}$ is the rotational generator for the scalar part of a field and the latter part $\hat{\mathbf{S}}$ generates rotation of the vector basis. Explicit expressions for Y_{lm}^N can be found in [6]. Eigenvalue equations are as below

$$\hat{J}_z \mathbf{Y}_{lm}^N = m \mathbf{Y}_{lm}^N \quad (\text{A.4})$$

$$\hat{J}^2 \mathbf{Y}_{lm}^N = l(l+1) \mathbf{Y}_{lm}^N \quad (\text{A.5})$$

The set of all tensor GSHs of a particular rank form a complete basis for tensor fields of the same rank in 3D space. Hence, a tensor field $F(\mathbf{r})$ of rank M can be decomposed as

$$\mathbf{F}(\mathbf{r}) = \sum_{s=0}^{\infty} \sum_{t=-s}^s \sum_{\mu=-M}^M F_{st}^{\mu}(r) \mathbf{Y}_{st}^{\mu} \quad (\text{A.6})$$

where $F_{st}^{\mu}(r)$ are its purely radially dependent GSH components.

A.2 Conventions

$$\gamma_l \equiv \sqrt{\frac{2l+1}{4\pi}} \quad (\text{A.7})$$

$$\Omega_l^N \equiv \sqrt{\frac{(l+N)(l-N+1)}{2}} \quad (\text{A.8})$$

Note that $\Omega_l^{-N} = \Omega_l^{N+1}$.

$$g_{\mu\nu} \equiv \hat{\mathbf{e}}_{\mu} \cdot \hat{\mathbf{e}}_{\nu} = \begin{pmatrix} 0 & 0 & -1 \\ 0 & 1 & 0 \\ -1 & 0 & 0 \end{pmatrix} \quad (\text{A.9})$$

where indices in the matrix run as $(-, 0, +)$.

$$\hat{\mathbf{e}}_{\mu}^* \cdot \hat{\mathbf{e}}_{\nu} = \delta_{\mu\nu} \quad (\text{A.10})$$

A.3 Spherical triple integral

$$\int_0^{2\pi} d\phi \int_0^{\pi} d\theta \sin \theta Y_{l_1 m_1}^{N_1} Y_{l_2 m_2}^{N_2} Y_{l_3 m_3}^{N_3} = 4\pi \gamma_{l_1} \gamma_{l_2} \gamma_{l_3} \begin{pmatrix} l_1 & l_2 & l_3 \\ N_1 & N_2 & N_3 \end{pmatrix} \begin{pmatrix} l_1 & l_2 & l_3 \\ m_1 & m_2 & m_3 \end{pmatrix} \quad (\text{A.11})$$

Explicit expressions for $\begin{pmatrix} l_1 & l_2 & l_3 \\ m_1 & m_2 & m_3 \end{pmatrix}$ can be found in [6]. The property $(Y_{lm}^N)^* = (-1)^{m+N} Y_{l\bar{m}}^{\bar{N}}$ makes it useful while taking inner products of tensor fields in our analysis. Note that works like [5], [12] etc. use a slightly different convention defining Y_{lm}^N as Y_{lm}^N / γ_l as in our convention. In this work, we have followed the convention of [6].

A.4 Rotation

Tensor GSH functions \mathbf{Y}_{lm}^N obey the same rotation laws as spherical harmonics Y_l^m . Consider two coordinates systems on a sphere (θ, ϕ) and (θ', ϕ') such that $\phi = 0$ and $\phi' = 0$ planes coincide. Also, for all points on this plane, let $\theta' = \theta - \beta$. This transformation law corresponds to the primed axis being tilted with respect to the unprimed axis by an angle β . Tensor GSH functions in the two coordinates are related as follows

$$\mathbf{Y}_{lm}^N(\theta', \phi') = \sum_{m'=-l}^l d_{mm'}^{(l)}(\beta) \mathbf{Y}_{lm'}^N(\theta, \phi) \quad (\text{A.12})$$

Generalised Spherical Harmonics Formalism

where $d_{mm'}^{(l)}$ is a $(2l+1) \times (2l+1)$ real matrix. Explicit form of $d_{mm'}^{(l)}$ can be found in [6] and a python subroutine for calculating this can be found in *functions.py* in the Github repository [14]. Above relation holds for all points on the entire sphere.